https://doi.org/10.5194/egusphere-2026-5331
Preprint. Discussion started: 19 October 2026
© Author(s) 2026. CC BY 4.0 License.

Dynamics of Coastal Permafrost Thaw Driven by Seawater Intrusion: A Numerical Study of Coupled Heat, Salt, and Groundwater Flow Processes

Tianyuan Zheng[1,2,3]*, Yucheng Lin[1,2,3], Shaobo Gao[1,2,3], Xilai Zheng[1,2,3], Rainer Helmig[1,2,3,4], Jian Luo[5]**

[1] College of Environmental Science and Engineering, Ocean University of China, Qingdao, China, Qingdao 266100, China.

[2] Key Laboratory of Marine Environment and Ecology, Ministry of Education, Ocean University of China, Qingdao 266100, China.

[3] Shandong Provincial Key Laboratory of Marine Engineering Geology and the Environment, Ocean University of China, Qingdao 266100, China.

[4] Institute for Modelling Hydraulic and Environmental Systems (IWS), Department of Hydromechanics and Modelling of Hydrosystems, University of Stuttgart, Pfaffenwaldring 61, Stuttgart, D-70569, Germany

[5] School of Civil and Environmental Engineering, Georgia Institute of Technology, Atlanta, GA 30332, USA.

Corresponding author: Tianyuan Zheng (zhengtianyuan@ouc.edu.cn);
Shaobo Gao (gaoshaobo@ouc.edu.cn)

https://doi.org/10.5194/egusphere-2026-5331
Preprint. Discussion started: 19 October 2026
© Author(s) 2026. CC BY 4.0 License.



Abstract: Global warming poses a growing threat to permafrost stability worldwide. Coastal permafrost is especially vulnerable because it is exposed to both rising ocean temperatures and seawater intrusion. However, the dynamic thermo-hydro-saline coupling mechanisms governing seawater intrusion-driven permafrost thaw remain poorly understood. This study employs a fully coupled groundwater (ice)-salt-heat numerical model to investigate these dynamics in a high-latitude coastal aquifer, with sensitivity analyses on seawater temperature, aquifer permeability, and porosity. Results identify seawater temperature (T_s) as the primary driver, with permafrost thaw volume increasing by ~105% as T_s rises from 0.5 to 3.5 °C. The system evolves from an initial density-driven, clockwise saline circulation to a mature double-circulation pattern, including a thermally-driven counterclockwise cell. The onset of this double circulation occurs earlier at higher T_s, fundamentally reshaping long-term heat transfer. The salt contribution degree (CD_s < 0.5) confirms thermal forcing dominates thaw, while salinity modulates early-phase thawing. Aquifer properties strongly modulate thaw sensitivity: higher permeability accelerates heat and solute transport but promotes earlier counterclockwise circulation development, which can limit inland advance. These findings quantify the nonlinear response of coastal permafrost to ocean warming and provide a predictive framework for assessing carbon mobilization and geotechnical risks in vulnerable Arctic regions.

Keywords: Seawater intrusion; Coastal aquifer; Numerical simulation; Coastal permafrost; Seawater temperature

https://doi.org/10.5194/egusphere-2026-5331
Preprint. Discussion started: 19 October 2026
© Author(s) 2026. CC BY 4.0 License.

1. Introduction

Permafrost is ground that remains at or below 0°C for at least two consecutive years and may contain variable amounts of ground ice. Its formation and spatial distribution are jointly controlled by regional climate and topographic conditions. Permafrost occupies a substantial fraction of Northern Hemisphere land, primarily at high latitudes and in high-altitude environments (Steinert et al., 2023; Devoie et al., 2024). These regions store vast amounts of organic carbon, and their stability plays a crucial role in regulating the global climate system and ensuring regional ecological security (Jones et al., 2023; Hjort et al., 2022).

Global temperatures have risen rapidly in recent decades, driven by anthropogenic greenhouse gas emissions that have altered Earth's energy balance (Lindsey & Dahlman, 2020). A substantial portion of the excess heat has been absorbed by the ocean, leading to continuous increases in oceanic heat content that extend to depths of nearly 3,000 m (Johnson & Lyman, 2020; Pachauri & Reisinger, 2007). Warming is particularly pronounced at high latitudes due to "polar amplification", with Arctic temperatures projected to rise by up to 8.3°C by 2100, potentially inducing widespread permafrost thaw (Lindsey & Dahlman, 2020; England et al., 2021; Zhou et al., 2024; Larsen et al., 2021; Lamontagne-Hallé et al., 2020). As permafrost thaws from the surface downward, subsurface hydraulic connectivity increases, activating groundwater flow systems (Walvoord & Kurylyk, 2016; Frampton & Destouni, 2015). Recent field and modeling evidence from the Alaskan Beaufort Sea coast demonstrates that this thaw-activated groundwater flow can mobilize substantial dissolved organic carbon, nitrogen, and CO_2 from coastal permafrost to adjacent lagoons and shelf waters (Demir et al., 2024).

Among the multiple drivers of coastal permafrost degradation, seawater intrusion is a critical

https://doi.org/10.5194/egusphere-2026-5331
Preprint. Discussion started: 19 October 2026
© Author(s) 2026. CC BY 4.0 License.

yet poorly understood physical process. Traditional studies of seawater intrusion have focused on temperate and tropical aquifers (e.g., Kuan et al., 2019; Lu et al., 2016), where density-driven flow under isothermal conditions dominates saltwater wedge formation and circulation (e.g., Robinson et al., 2007). More recent work has shown that non-isothermal conditions can substantially alter these classical patterns (Nguyen et al., 2020). For example, Pu et al. (2020) demonstrated that a lower saltwater circulation cell may form only when seawater is warmer than freshwater, whereas such a circulation does not form under isothermal conditions or when seawater is colder than freshwater. This asymmetry arises because thermal diffusivity exceeds solute diffusivity, causing temperature-driven buoyancy effects to evolve differently from salinity-driven density contrasts. The manifestation of these differential transport processes is fundamentally controlled by the water retention properties and microstructure of the porous medium, which govern how heat and solutes move and interact. For instance, Xu et al. (2024) provide foundational insights into how sediment depth influences the hysteresis of water retention, elucidating how wetting paths and pore structure characteristics control moisture states across scales. This highlights that intrinsic material properties, such as permeability and porosity, are critical when modeling the coupled thermo-hydro-saline dynamics in frozen systems. Despite these advances, existing theoretical frameworks remain difficult to extrapolate to cold coastal environments, where strong temperature gradients, ice-water phase change, and salinity-dependent freezing-point depression introduce tightly coupled water-heat-salt processes.

High-latitude coastal permafrost situated at the land-sea interface is therefore subjected to both atmospheric warming and marine forcing. Rising sea levels displace the freshwater-saltwater interface landward, facilitating seawater intrusion into coastal aquifers (Werner et al., 2013). Where

https://doi.org/10.5194/egusphere-2026-5331
Preprint. Discussion started: 19 October 2026
© Author(s) 2026. CC BY 4.0 License.

pore ice saturation is incomplete, saltwater can infiltrate unfrozen pore spaces, lower freezing temperatures, and initiate thaw (Harrison & Osterkamp, 1978). Thawing can increase hydraulic conductivity by several orders of magnitude, accelerating saltwater flow and creating a positive feedback that enhances further permafrost degradation (Watanabe & Osada, 2016). Although basal seawater intrusion, defined as the upward migration of warm, saline water from beneath the permafrost base into the frozen sediment, can drive sustained permafrost thaw (Frederick & Buffett, 2015; Angelopoulos et al., 2019), limited subsurface observations hinder direct quantification of its spatial extent and impact.

To overcome observational constraints, recent studies have employed numerical modeling, remote sensing, and geophysical methods. Guimond et al. (2021) developed a coupled groundwater (ice) – salt – heat numerical model and demonstrated that seawater intrusion drives lateral permafrost retreat, with the thaw front extending farther inland under saline conditions than under freshwater-only conditions. Geophysical surveys from Svalbard coastal sites indicate that seawater can modify the base of coastal permafrost, supporting the concept of a "bottom active layer" where basal warming promotes thaw from below (Kasprzak et al., 2017). Despite these advances, systematic understanding of the underlying thermo-hydro-saline coupling mechanisms remains limited (Fig. 1). Key uncertainties include the evolution of subsurface flow fields under combined thermal and salinity forcing, the potential formation of double circulation structures under phase-change conditions (which have been previously identified in non-frozen aquifers by Pu et al., 2020), and the sensitivity of thaw dynamics to ocean temperature and aquifer properties. Moreover, although fully coupled frameworks exist (e.g., Guimond et al., 2021), the relative contributions of thermal and salinity effects have not been systematically quantified across a range of ocean

https://doi.org/10.5194/egusphere-2026-5331
Preprint. Discussion started: 19 October 2026
© Author(s) 2026. CC BY 4.0 License.

temperatures and aquifer properties, constraining predictive capability over decadal to centennial timescales.

To address these gaps, this study develops a fully coupled groundwater (ice) – salt – heat numerical model for cold coastal environments. The objectives are to: (1) elucidate the thermo-hydro-saline coupling dynamics of permafrost thaw driven by seawater intrusion; (2) quantify the relative contributions of thermal and salinity effects under different ocean temperature scenarios and aquifer property ranges; and (3) reveal how permeability and porosity regulate thaw rates, thaw-front advance, and the onset of double circulation. By advancing the mechanistic understanding of these coupled processes, this work provides a robust scientific basis for predicting the evolution of coastal permafrost under climate change.

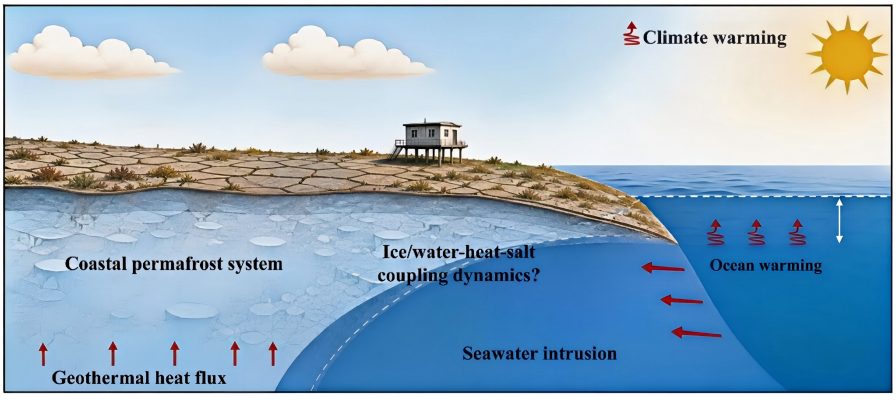


Fig. 1. Schematic diagram illustrating the coupled multiphysics processes within a coastal permafrost system with seawater warming.

2. Materials and Methods

2.1. Conceptual Model

Seawater intrusion induces coastal permafrost thawing, a process that involves complex, coupled interactions among thermal, phase change, fluid flow, and solute concentration fields. To

https://doi.org/10.5194/egusphere-2026-5331
Preprint. Discussion started: 19 October 2026
© Author(s) 2026. CC BY 4.0 License.

make the problem tractable, we adopted the following simplifying assumptions: (1) the aquifer is unconfined, homogeneous, and isotropic; (2) it is fully saturated; (3) the intrinsic permeability and porosity remain constant, while thaw-induced changes in effective hydraulic conductivity are represented solely by the saturation-dependent relative permeability; (4) the influence of seasonal freeze-thaw cycles is not considered; (5) regarding salt transport, we assume that the solute dispersion coefficient is constant within the simulation domain, and the effect of salt adsorption by porous media particles is negligible (consistent with the common assumptions in coastal cryohydrogeological simulations, Guimond et al., 2021).

The conceptual model represents a high-latitude coastal subsurface region measuring 500 m in length and 50 m in depth (Fig. 2). The top boundary is impermeable and has a prescribed constant temperature to simulate the insulating effect of snow cover. The bottom boundary is defined as a geothermal heat flux boundary (0.05 W/m²), representing the regional geothermal background. The left (inland) boundary is hydraulically impermeable. The right-side (ocean) boundary has a constant salt concentration of 36 g/L, a prescribed hydraulic head (h_s = 47 m), and a constant temperature.

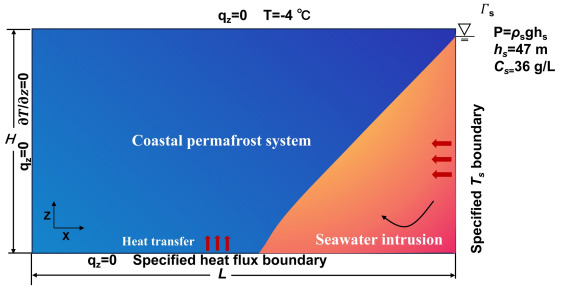


Fig. 2. Cross-section domain and boundary conditions for the numerical model of a coastal permafrost system.

2.2. Governing Equations

Based on the conceptual model and assumptions in Section 2.1, the seawater-intrusion-driven

https://doi.org/10.5194/egusphere-2026-5331
Preprint. Discussion started: 19 October 2026
© Author(s) 2026. CC BY 4.0 License.

coastal permafrost thaw is governed by coupled variable-density fluid flow, multiphase heat and mass transfer, and solute transport. This coupled system is described by the following three partial differential equations.

The governing equation for variable-density groundwater flow in the unconfined aquifer is given by:

$$\nabla \cdot [\frac{\rho_w g k_{rw}(S_w)\mathbf{k}}{u} \nabla(\rho_f(T,c) \cdot [h_f + \frac{\rho_f - \rho_w}{\rho_w} z])] = \rho_f(T,c) \cdot [S_w n \beta \rho_w g] \frac{\partial h_f}{\partial t} \quad (1)$$

where ρ_f is the fluid density [kg/m^3]; g is the gravitational acceleration constant [m/s^2]; k_{rw} is the relative permeability [-]; $\mathbf{k}$ is the intrinsic permeability tensor of the aquifer [m^2]; h_f is the equivalent freshwater hydraulic head [m]; z is the elevation [m]; u is the fluid viscosity [kg/(m·s)]; β is the aquifer compressibility [m·s^2/kg]; t is time [s]; n is porosity [-]; S_w is the water saturation [-]; and ρ_w is the freshwater density [kg/m^3]. It should be clarified that ρ_w is a constant (1000 kg/m^3) in this study, while ρ_f is a function of temperature and salinity, which is specifically described by Equation 7 (nonlinear equation of state). ρ_w is not dependent on other variables, and this distinction is intended to avoid confusion in the expression of density dependencies. Regarding u: the seawater temperature simulated in this study ranges from 0.5 to 3.5 ℃, and the subsurface temperature difference is small (within 5 ℃). According to the physical properties of water and relevant literature (Guimond et al., 2021; Bense et al., 2009), the viscosity of water changes minimally within such a narrow temperature range. Therefore, u is assumed to be a constant in this study and is not formulated as a function of temperature.

The relative permeability k_{rw} is defined as a function of water saturation S_w (McKenzie et al., 2007; Guimond et al., 2021):

https://doi.org/10.5194/egusphere-2026-5331
Preprint. Discussion started: 19 October 2026
© Author(s) 2026. CC BY 4.0 License.

$$k_{rw}(S_w) = \max(10^{-n\Omega(1-S_w)}, 10^{-6}) \quad (2)$$

where Ω is an impedance factor [-].

The governing equation for heat transfer (Bense et al., 2009), which incorporates latent heat effects from pore ice thawing/freezing, is shown below :

$$\nabla \cdot [\kappa_e \nabla T] - \rho_w C_w \nabla \cdot (vT) = C_p \frac{\partial T}{\partial t} + nL_i \frac{\partial S_w}{\partial t} \quad (3)$$

where κ_e is the effective thermal conductivity of the sediment/fluid/ice mixture [W/(m·°C)]; C_w is the volumetric water heat capacity [J/(kg·°C)]; T is subsurface temperature [°C]; v is the pore water velocity vector [m/s]; L_i is the volumetric latent heat of fusion [J/m^3]; and C_p is the volumetric heat capacity [J/(kg·°C)]. The expression for C_p follows Guimond et al. (2021).The effective thermal conductivity κ_e is determined by:

$$\kappa_e = nS_w\kappa_w + n(1-S_w)\kappa_i + (1-n)\kappa_s \quad (4)$$

where κ_w is the thermal conductivity of water [W/(m·°C)]; κ_i is the thermal conductivity of ice [W/(m·°C)]; and κ_s is the thermal conductivity of solids [W/(m·°C)]. Under the assumption that the pore space is occupied only by liquid water and ice, the phase saturations satisfy $S_w + S_i = 1$. Consequently, S_i is determined by Equation 6 once T and c are specified and is not independently calculated from ρ_i. The phase-volume fractions entering Equation 4 are nS_w for liquid water, nS_i for ice, and 1-n for the solid matrix. The ice density ρ_i (listed in Table 1, 920 kg/m^3) is used to convert the bulk volumetric ice content into ice mass. Specifically, the ice volume per unit bulk volume is $\theta_i = nS_i$, and the corresponding ice mass per unit bulk volume is $M_i = \rho_i nS_i$. Therefore, ρ_i does not independently regulate S_i or κ_e in Equation 4; instead, the different thermal conductivities of ice, water, and solids affect κ_e through their respective phase-volume fractions.

The governing equation for solute transport is given by:

https://doi.org/10.5194/egusphere-2026-5331
Preprint. Discussion started: 19 October 2026
© Author(s) 2026. CC BY 4.0 License.

$$\nabla \cdot [nS_w \mathbf{D} \nabla c] - \nabla \cdot (vc) = nS_w \frac{\partial c}{\partial t} \tag{5}$$

where **D** is the hydrodynamic dispersion coefficient tensor [m²/s] and c is the solute concentration, which in this study refers specifically to the salt concentration [kg/m³]. Fluid density is not included as an independent transported variable in Equation 5. Instead, changes in ρ_f caused by temperature and salt concentration affect salt transport through the groundwater-flow field calculated from Equation 1, thereby influencing the advective and dispersive salt fluxes.

To account for the freezing point depression caused by increased osmotic potential, a salinity- and temperature-dependent soil freezing characteristic (SFC) curve is introduced. The relationship between liquid water and ice based on temperature and salinity is described by:

$$S_w = (1 - S_{wres}) e^{-(\frac{T}{W(c)})^2} + S_{wres} \tag{6}$$

where S_{wres} is the residual water content [-], and $W(c)$ is a fitting parameter for the SFC curve. A linear interpolation method is employed to determine the influence of salinity on the freezing point depression (Mohammed et al., 2021). This equation ensures the existence of residual pore water even when the soil is completely frozen and accounts for the effect of different salinities on water saturation. Based on the principle of mass conservation, the sum of water saturation and ice saturation is unity; therefore, the pore ice content is determined once the saturations are known.

The density variation induced by temperature and salinity is described by a nonlinear equation of state (Nguyen et al., 2020):

$$\begin{aligned} \rho_f(T,c) = {} & (999.9 + 2.034\times10^{-2}T - 6.162\times10^{-3}T^2 + 2.261\times10^{-5}T^3 \\ & -4.657\times10^{-8}T^4) + (0.802c - 2.001\times10^{-3}cT + 1.677\times10^{-5}cT^2 \\ & -3.06\times10^{-8}cT^3 - 1.613\times10^{-8}c^2T^2) \end{aligned} \tag{7}$$

2.3. Numerical Simulations

The governing partial differential equations for variable-density flow, heat transfer, and solute

https://doi.org/10.5194/egusphere-2026-5331
Preprint. Discussion started: 19 October 2026
© Author(s) 2026. CC BY 4.0 License.

transport (Section 2.2) were solved numerically using the finite element method within the COMSOL Multiphysics® (v6.1) software environment. This platform facilitates a fully coupled, monolithic approach for addressing the multiphysics nature of the problem. The numerical implementation in COMSOL was designed to robustly handle the strong nonlinearities and tight coupling between the governing processes, ensuring a consistent and accurate representation of the underlying physics. This established numerical framework provided a reliable basis for the subsequent sensitivity and scenario analyses conducted in this study.

The simulation comprised two sequential stress periods to represent distinct phases of permafrost evolution: (1) permafrost formation and (2) seawater-intrusion-driven thaw. In the first stress period (permafrost formation), the domain was initialized with a uniform freshwater hydraulic head of 48.5 m, a salt concentration of 0 g/L, and a deliberately high uniform temperature of 20°C to accelerate convergence toward steady state. A constant temperature of -4 °C was prescribed at the top boundary to represent the insulating effect of snow cover, and a constant geothermal heat flux of 0.05 W/m^2 was applied at the bottom boundary. During this 100,000-day spin-up, the initially warm domain gradually cooled under these boundary conditions until a stable permafrost configuration was achieved. No salt was introduced during this stage, so the salt concentration remained uniformly zero at the end of the first period. The final steady-state distributions of hydraulic head, temperature, and ice saturation served as the initial conditions for the second stress period. In the second stress period (seawater intrusion and thaw), the simulation continued for an additional 60,000 days. For consistency across scenarios, the spatial fields and time-series plots are shown through 50,000 days, whereas double saltwater circulation onset time (t_{dc}) values were diagnosed from the full 60,000-day simulations. Thaw was initiated by abruptly imposing a constant

https://doi.org/10.5194/egusphere-2026-5331
Preprint. Discussion started: 19 October 2026
© Author(s) 2026. CC BY 4.0 License.

seawater salinity of 36 g/L and a prescribed seawater temperature at the right-side (ocean) boundary, while maintaining the top and bottom thermal boundaries unchanged. The sudden exposure to warm, saline water drove both thermal and haline perturbations into the permafrost system, triggering basal thaw and the subsequent coupled thermo-hydro-saline dynamics analyzed in this study. The model parameters were assigned based on literature values for typical Arctic coastal sediments and are summarized in Table 1.

Four sets of numerical simulations were performed to examine how seawater intrusion affects permafrost under varying conditions (Table 2). For the base case (Case 1), permeability and porosity were set to 10^{-11} m^2 and 0.4, respectively, to represent dense sandstone. Seawater temperature was fixed at 1.5 °C, the mean ocean temperature in high-latitude coastal areas, to analyze the spatiotemporal patterns of seawater-induced permafrost thaw. Set 2 (Cases 2-5) evaluated the impact of ocean temperature on both seawater intrusion and permafrost thaw. Four seawater temperatures (Ts = 0.5, 1.5, 2.5, and 3.5 °C) were tested. Set 3 (Cases 6-10) investigated how aquifer permeability influences permafrost thaw by simulating five values (k=1×10^{-12}, 5×10^{-12}, 1×10^{-11}, 5×10^{-11}, and 1×10^{-10} m^2), covering low-, medium-, and high-permeability regimes. Set 4 (Cases 11-14) assessed permafrost-thaw variations across four aquifer-porosity values (n = 0.25, 0.30, 0.35, 0.40). To isolate the role of salinity, a salt-free counterpart was included in every simulation set.

2.4. Evaluation Metrics

Temporal and spatial changes in permafrost thaw volume and solute concentration fields are analyzed to assess the impact of seawater intrusion on coastal permafrost dynamics. The actual thaw volume of permafrost (PV) serves as the primary indicator of degradation, with permafrost defined as regions where ice saturation exceeds 30% of the pore space. To isolate the influence of salinity,

https://doi.org/10.5194/egusphere-2026-5331
Preprint. Discussion started: 19 October 2026
© Author(s) 2026. CC BY 4.0 License.

the salt contribution degree (CD_s) is introduced as a dimensionless constant:

$$CD_s = \frac{PV - PV_f}{PV} \tag{8}$$

where PV and PV_f are the thaw volumes under seawater and freshwater conditions, respectively. $CD_s > 0$ indicates that salinity promotes permafrost thaw, while $CD_s = 0$ suggests no salinity effect.

Spatial changes are evaluated using three distance-based metrics measured from the seaward boundary. The saltwater wedge length (*SWL*) is defined as the point where the 0.1 isochlor (i.e., 10% seawater salinity) intersects the impermeable aquifer base. The thawing front distance (*TFD*) characterizes the extent of basal thaw, defined as the point where the thaw front (the interface between thawed and frozen ground) intersects the aquifer base. The 0 °C isotherm distance (*TID*) tracks the evolution of the thermal field, defined as the point where the 0 °C isotherm intersects the aquifer base.

In this study, the relative positions of *TFD* and *TID* with respect to *SWL* are critical for understanding the coupling between solute transport and heat transfer. When *TFD* > *SWL*, it indicates that the thaw front has advanced beyond the saline plume, suggesting that thermal conduction dominates the thaw process in that region.

Table 1 Numerical parameters adapted from Guimond et al., 2021 (a); Gao et al., 2025 (b); Bense et al., 2009, 2012 (c).

Parameters	Values	Unit
Model domain length, L	500	[m]
Model domain height, H	50	[m]
Aquifer compressibility*, β	1.0×10^{-8}	[m·s²/kg]

https://doi.org/10.5194/egusphere-2026-5331
Preprint. Discussion started: 19 October 2026
© Author(s) 2026. CC BY 4.0 License.

Freshwater density, ρ_w	1000[a]	[kg/m^3]
Ice density, ρ_i	920	[kg/m^3]
Solid grain density, ρ_s	2650[a]	[kg/m^3]
Thermal conductivity of water, κ_w	0.6[a]	[W/(m·°C)]
Thermal conductivity of ice, κ_i	2.14[a]	[W/(m·°C)]
Thermal conductivity of solids, κ_s	3.5[a]	[W/(m·°C)]
Impedance factor, Ω	50[a]	[-]
Longitudinal dispersivity, α_L	1[b]	[m]
Transverse dispersivity, α_T	0.1*α_L[b]	[m]
Volumetric latent heat of fusion, L_i	3.03×10^8[c]	[J/m^3]
Specific heat of ice, c_i	2060[a]	[J/(kg·°C)]
Specific heat of water, c_w	4182[a]	[J/(kg·°C)]
Specific heat of solid grains, c_s	835[a]	[J/(kg·°C)]
Residual saturation, S_{wres}	0.05[a]	[-]
Ocean temperature, T_s	0.5, **1.5**[**], 2.5, 3.5	[°C]
Intrinsic permeability, k	1×10^{-12}, 5×10^{-12}, **1×10^{-11}**[**], 5×10^{-11}, 1×10^{-10}	[m^2]
Porosity, n	0.25, 0.3, 0.35, **0.4**[**]	[-]

[*] β incorporates the compressibility of both water and the matrix.

[**] Boldfaced numbers with an underline are the reference values of T_s, k and n.

https://doi.org/10.5194/egusphere-2026-5331
Preprint. Discussion started: 19 October 2026
© Author(s) 2026. CC BY 4.0 License.

261 Table 2 Sensitivity analysis parameters and double saltwater circulation onset time (t_{dc}).

Set	Case	T_s (℃)	k (m²)	n (-)	t_{dc} (×10³ d)
1	1	1.5	1×10^{-11}	0.40	37
2	2	0.5	1×10^{-11}	0.40	55
	3	1.5	1×10^{-11}	0.40	37
	4	2.5	1×10^{-11}	0.40	30
	5	3.5	1×10^{-11}	0.40	25
	6	1.5	1×10^{-12}	0.40	-
	7	1.5	5×10^{-12}	0.40	58
3	8	1.5	1×10^{-11}	0.40	37
	9	1.5	5×10^{-11}	0.40	14
	10	1.5	1×10^{-10}	0.40	12
4	11	1.5	1×10^{-11}	0.25	21
	12	1.5	1×10^{-11}	0.30	26
	13	1.5	1×10^{-11}	0.35	31
	14	1.5	1×10^{-11}	0.40	37

262 Note: Cases 1, 3, 8, and 14 represent the identical base case and are repeated here for clarity under

263 each sensitivity analysis set.

264

https://doi.org/10.5194/egusphere-2026-5331
Preprint. Discussion started: 19 October 2026
© Author(s) 2026. CC BY 4.0 License.

3. Results

3.1. Spatiotemporal evolution of permafrost thaw under seawater intrusion

Fig. 3 depicts the coupled evolution of salinity, flow, phase-change, and temperature fields in a coastal permafrost system under baseline conditions. At the initial intrusion stage (t = 1000 d), the salinity field shows a vertically upward, clockwise circulation of saline water, which forms a high-salinity accumulation zone at the aquifer base (Fig. $3a_1$). This flow pattern is primarily driven by the density contrast between seawater and resident pore water. Concurrently, the intrusion of relatively warm seawater induces thermal thawing of the permafrost. The phase-change field (Fig. $3a_2$) indicates that the thaw zone advances in a near-planar manner, with its spatial extent closely matching the region above the 0°C isotherm in the temperature field (Fig. $3a_3$). This suggests that the initial permafrost thaw is predominantly controlled by the thermal gradient between the marine environment and the aquifer.

As the system evolves to t = 10,000 d, the formation of a coastal thaw zone increases the effective hydraulic conductivity through the saturation-dependent relative-permeability term $k_{rw}(S_w)$, thereby facilitating saline-water flow, while the intrinsic permeability k remains constant. The flow path shifts to near-horizontal migration followed by upward discharge (Fig. $3b_1$). Because discharge occurs along the saline water front—which coincides with the thaw front—the upward saline circulation further enhances thermal thawing. The saltwater wedge at this stage exhibits a distinct "bulging" morphology, resulting from the flow-blocking effect of the permafrost, which forces saline water to continuously thaw the surrounding ice through internal circulation. Consequently, the freshwater-saltwater interface markedly differs from the classic saltwater wedge morphology observed in temperate regions (e.g., Lu et al., 2016; Kuan et al., 2019). The phase-change field (Fig.

https://doi.org/10.5194/egusphere-2026-5331
Preprint. Discussion started: 19 October 2026
© Author(s) 2026. CC BY 4.0 License.



287 3b$_2$) shows that the thaw zone aligns closely with the saltwater wedge, which is consistent with
288 strengthened thermal-solute coupling under the present boundary conditions. In the temperature
289 field (Fig. 3b$_3$), the 0°C isotherm diverges between the upper and lower aquifer. In the upper section,
290 enhanced permeability and faster flow in the thawed zone intensify thermal convection, creating a
291 relatively high-temperature region. In contrast, the lower section remains dominated by thermal
292 conduction.

293 During the long-term evolution stage (t = 50,000 d), the saltwater wedge continues to lengthen.
294 Notably, the flow pattern at the aquifer base undergoes a significant transformation: a reversed,
295 counterclockwise secondary circulation develops beneath the primary density-driven circulation
296 (Fig. 3c$_1$). Throughout this period, the transition zone between saline water and freshwater or ice
297 remains narrow (Figs. 3b$_1$, c$_1$). This narrowness stems from two mechanisms: (1) the permafrost
298 acts as a physical barrier, impeding solute dispersion and restricting lateral groundwater flow,
299 thereby limiting saline water spreading; and (2) continuous seawater replenishment maintains a
300 high-salinity core within the aquifer. The phase-change field (Fig. 3c$_2$) indicates that under sustained
301 marine heat input, permafrost thaw continues, and the thaw zone morphology remains highly
302 synchronized with the saltwater wedge. In the temperature field (Fig. 3c$_3$), the position of the 0°C
303 isotherm changes little (*TID* increases from 14.28 m to 15.72 m), and the spatial distribution of the
304 high-temperature region shows no significant alteration. This is attributed to the reversal of the basal
305 saline flow direction, which attenuates inland-directed thermal convection and thus diminishes heat
306 transfer. Furthermore, the continuous water-saturation distribution in the phase-change field reveals
307 a narrow active layer between the thawed and frozen zones, whose morphology essentially coincides
308 with the freshwater-saltwater/ice transition zone.

https://doi.org/10.5194/egusphere-2026-5331
Preprint. Discussion started: 19 October 2026
© Author(s) 2026. CC BY 4.0 License.

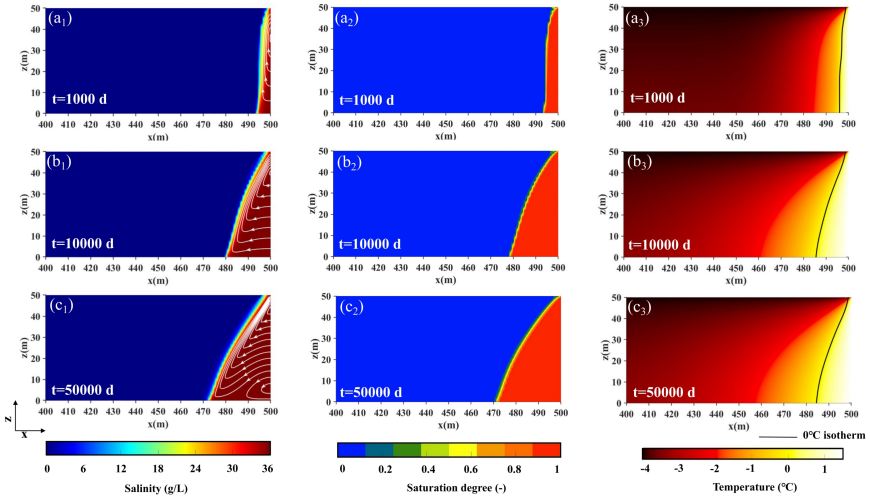


Fig. 3. Temporal evolution of coupled flow-salinity fields, water saturation, and temperature distributions under baseline conditions (Case 1). Panels (a_1-a_3) correspond to t = 1000 d, (b_1-b_3) to t = 10000 d, and (c_1-c_3) to t = 50000 d, showing the flow-salinity field, water saturation, and temperature field, respectively. White streamlines in (a_1, b_1 and c_1) denote saltwater flow paths. Black lines in (a_3, b_3 and c_3) mark the 0 °C isotherm.

The actual permafrost thaw volume (*PV*) exhibits a characteristic two-stage evolution of "rapid-quasi-steady" phases over time (Fig. 4a). During the initial 5,000 days, driven by the pronounced temperature gradient between the ocean and the aquifer, thermal convection dominates the thawing process, with a thaw rate as high as 103.87 m² per thousand days, marking the rapid thawing phase. This phase corresponds to the system's adjustment from an initial steady state to a new stressed condition, as depicted in the early evolution of flow and temperature fields in Fig. 3. Subsequently, the *PV* increment stabilizes, entering a stable thawing phase, indicating continued thawing at a controlled rate and reflecting a dynamic equilibrium between driving forces and feedback mechanisms. The salt contribution degree (CD_s) shows a unimodal trend, first increasing

https://doi.org/10.5194/egusphere-2026-5331
Preprint. Discussion started: 19 October 2026
© Author(s) 2026. CC BY 4.0 License.

and then decreasing. This is attributed to the early evolution stage, where saline water forms a clockwise single circulation cell within the newly developed thaw zone (consistent with the flow pattern shown in Fig. $3a_1$), continuously transporting salt to the permafrost-thaw zone interface. The depression of the porewater freezing point by salt promotes thawing, leading to a continuous rise in CD_s. As the system evolves further, the flow field gradually adjusts to a dual-circulation pattern that includes a counterclockwise cell. The onset time of this double saltwater circulation (t_{dc}) under baseline conditions is 37,000 days. This transition marks a key shift in solute transport dynamics: the counterclockwise cell (as seen in the long-term evolution in Fig. 3c1) causes some saline water to return seaward before reaching the permafrost zone, thereby reducing the direct salt contribution to thawing. The variation in CD_s highlights the critical role of "solute exclusion" and the evolution of flow patterns: salt promotes initial thawing by lowering the freezing point, while flow reorganization regulates solute transport pathways and efficiency. Overall, thermal forcing is the primary control on permafrost thawing, while salinity effects modulate the process by altering phase-change conditions.

The dynamic curves of the thawing front distance (*TFD*), saltwater wedge length (*SWL*), and 0 °C isotherm distance (*TID*) elucidate the multi-physical field coupling process (Fig. 4b). TFD and *SWL* show synchronous and continuous growth, consistent with the *PV* variation, confirming the direct control of saltwater intrusion on thaw front advance—a relationship visually supported by the corresponding alignment between the saltwater wedge in Figs. $3b_1$ and $3c_1$ and the thaw zone in Figs. $3b_2$ and $3c_2$. In the initial stage, driven by the temperature difference, continuous saltwater intrusion and phase change cause *SWL* to increase rapidly; as the flow pattern transitions (from the early clockwise cell to the later complex patterns in Fig. 3), its growth rate gradually decays to a

https://doi.org/10.5194/egusphere-2026-5331
Preprint. Discussion started: 19 October 2026
© Author(s) 2026. CC BY 4.0 License.

stable state. The significant positive correlation between *TFD* and *SWL* indicates that *SWL* can serve as an effective proxy for assessing lateral thawing extent; therefore, only the *TFD* curve is presented in subsequent sensitivity analyses. The change in *TID* is divided into two stages: a rapid advance phase and a slight retreat phase. In the initial stage, intense thermal convection—driven by the accumulation of high-density saline water at the aquifer base and enhanced permeability—promotes rapid inland migration of the 0 °C isotherm. In the later stage, the reversal of the basal saline flow direction to seaward (as shown in Fig. 3c_1) weakens thermal convection, causing *TID* movement to slow or even exhibit slight retreat. The differential evolution of *TFD*, *SWL*, and *TID* further indicates that the thawing process is jointly dominated by thermal conduction and convection, and that a lag and feedback exist between the geometric expansion of the saltwater wedge and the advance of the thermal front.

https://doi.org/10.5194/egusphere-2026-5331
Preprint. Discussion started: 19 October 2026
© Author(s) 2026. CC BY 4.0 License.

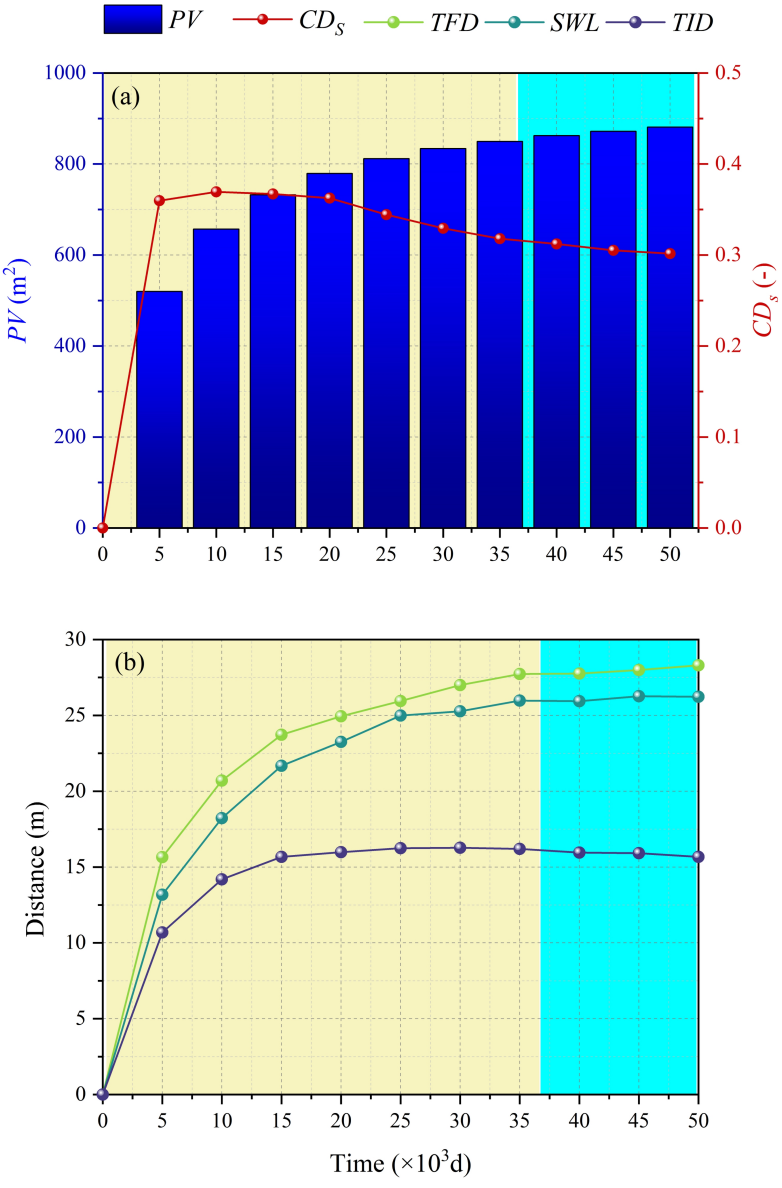


Fig. 4. Temporal variations of (a) the actual permafrost thaw volume (*PV*) and salt contribution degree (CD_s), as well as (b) the thawing front distance (*TFD*), saltwater wedge length (*SWL*), and 0 °C isotherm distance (*TID*). The ochre-shaded area represents the period when only a single (clockwise) saline circulation pattern occurs, while the sky-blue-shaded area corresponds to the period when a dual (clockwise and counterclockwise) saline circulation pattern develops.

https://doi.org/10.5194/egusphere-2026-5331
Preprint. Discussion started: 19 October 2026
© Author(s) 2026. CC BY 4.0 License.

3.2. Permafrost thaw dynamics driven by seawater temperature variations

This section extends the analysis of the baseline scenario (T_s = 1.5°C) from Section 3 to investigate how seawater intrusion influences permafrost thaw under varying T_s. Fig. 5 presents the salinity, flow, phase-change, and temperature fields at 50,000 days for T_s = 0.5°C, 1.5°C, 2.5°C, and 3.5°C. At T_s = 0.5°C (Fig. 5a_1), the saltwater wedge lacks the pronounced convex shape seen in the baseline (Fig. 5b_1), indicating weaker saline recirculation during thaw. In this cold scenario, seawater flow is dominated solely by density-driven, unidirectional (clockwise) recirculation, matching the early-stage pattern of baseline evolution (Fig. 3a_1). This implies that the development of a mature double-circulation cell—a key long-term feature resulting from coupled density- and thermally-driven convection—is inhibited under cold conditions. Correspondingly, the saltwater wedge shape closely resembles the thaw zone geometry (Fig. 5a_2), reflecting a simpler thermal-solute coupling where the thaw front is primarily shaped by density-driven flow. The 0°C isotherm approximates an inclined straight line (Fig. 5a_3), showing minimal vertical disparity in thaw extent. This is due to limited thermal input, which restricts thaw front advance and reduces saline accumulation in the lower aquifer—a process that enhances thermal convection in the baseline. Consequently, heat transfer efficiency is reduced, yielding a relatively uniform thermal field across the aquifer depth, unlike the vertically differentiated structure seen in the baseline (Fig. 5b_2).

Figs. 5c_1-d_1 depict the flow-concentration field in a coastal permafrost system under elevated ocean temperatures of 2.5°C and 3.5°C. Compared to the baseline conditions (Fig. 5b_1), as T_s increases, the saltwater wedge morphology becomes increasingly convex and prominent, signifying enhanced saline water recirculation intensity. Concurrently, the spatial extent of the double-circulation cell expands markedly. This confirms that the lower, counterclockwise secondary

https://doi.org/10.5194/egusphere-2026-5331
Preprint. Discussion started: 19 October 2026
© Author(s) 2026. CC BY 4.0 License.



385 circulation loop—initiated during the long-term baseline evolution stage (Fig. 3c$_1$)—is primarily
386 driven and intensified by thermal convection induced by warmer seawater, a pattern absent in the
387 low-temperature scenario (Fig. 5a$_1$). Moreover, the geometry of the permafrost thaw zone undergoes
388 significant alteration (Figs. 5c$_2$, d$_2$), with a growing disparity between the upper and lower thaw
389 extents. The increased heat flux from warmer seawater generates more extensive thawed regions,
390 promoting greater saline water accumulation in the lower aquifer. This accumulation strengthens
391 the density contrast and thermal convection, creating a positive feedback loop between solute
392 transport and heat transfer—a mechanism active but less pronounced in the baseline. In contrast,
393 the upper aquifer experiences slower thawing due to the insulating effect of the overlying ice-rich
394 permafrost and comparatively less saline water accumulation, leading to more pronounced vertical
395 differentiation in thaw rates. From a thermal perspective, the 0°C isotherm exhibits pronounced
396 vertical asymmetry (Figs. 5c$_3$, d$_3$), which intensifies with rising Ts. This further confirms that ocean
397 warming intensifies the thermal-solute coupling processes, thereby accelerating the positive
398 feedback between thawing and solute transport.
399

https://doi.org/10.5194/egusphere-2026-5331
Preprint. Discussion started: 19 October 2026
© Author(s) 2026. CC BY 4.0 License.

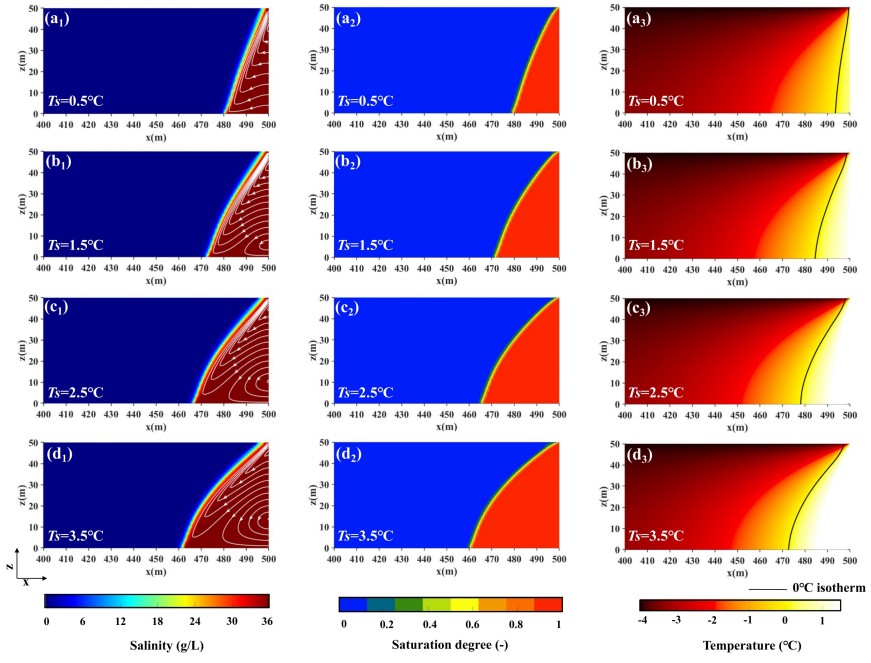


Fig. 5. Coupled flow-salinity fields, water saturation, and temperature distributions at 50,000 days under varying seawater temperatures (T_s). Panels (a_1-a_3) correspond to T_s = 0.5 °C, (b_1-b_3) to T_s = 1.5 °C, (c_1-c_3) to T_s = 2.5 °C, and (d_1-d_3) to T_s = 3.5 °C, showing the flow-salinity field, water saturation, and temperature field, respectively. White streamlines denote saltwater flow paths. Black lines mark the 0 °C isotherm.

Fig. 6a shows that permafrost thaw under varying seawater temperatures (T_s) follows a two-stage "rapid-quasi-steady" evolution, but with diverging dynamics from the outset. *PV* at 50,000 days increases with T_s (636.11, 901.36, 1116.7, and 1304.04 m^2 for T_s = 0.5, 1.5, 2.5, and 3.5°C), yet the incremental gains diminish (265.25, 215.34, and 187.34 m^2), indicating a weakening thaw response to warming. This trend is mirrored by *TFD* (Fig. 6b), which reaches 20.98, 28.88, 34.90, and 39.91 m at 50,000 days, with similarly decreasing increments (7.9, 6.02, and 5.01 m).

TID takes longer to stabilize under higher T_s (e.g., ~15,000 d at 0.5°C vs. ~22,000 d at 3.5°C),

https://doi.org/10.5194/egusphere-2026-5331
Preprint. Discussion started: 19 October 2026
© Author(s) 2026. CC BY 4.0 License.

413 reflecting intensified heat transfer (Fig. 6c). Notably, *TID* retreat occurs at $T_s \geq 1.5$°C and amplifies
414 with warming. This is linked to the earlier onset of the dual saltwater circulation pattern: the double
415 circulation onset time (t_{dc}) decreases from 55,000 d at $T_s = 0.5$°C to 37,000, 30,000, and 25,000 d at
416 $T_s = 1.5$, 2.5, and 3.5°C, respectively (Table 2). The earlier and enhanced lower (counterclockwise)
417 saline circulation at higher T_s weakens inland-directed thermal convection more rapidly, leading to
418 the observed *TID* retreat. CD_s remains below 0.5 in all cases, confirming thermal dominance (Fig.
419 6d). At $T_s = 0.5$°C, CD_s rises continuously due to persistent single (clockwise) circulation along the
420 thaw front. Under $T_s \geq 1.5$°C, the dual circulation pattern emerges, producing a unimodal CD_s trend;
421 higher T_s strengthens the lower (counterclockwise) cell, diverting saline water seaward and thus
422 reducing the final salt contribution.

https://doi.org/10.5194/egusphere-2026-5331
Preprint. Discussion started: 19 October 2026
© Author(s) 2026. CC BY 4.0 License.

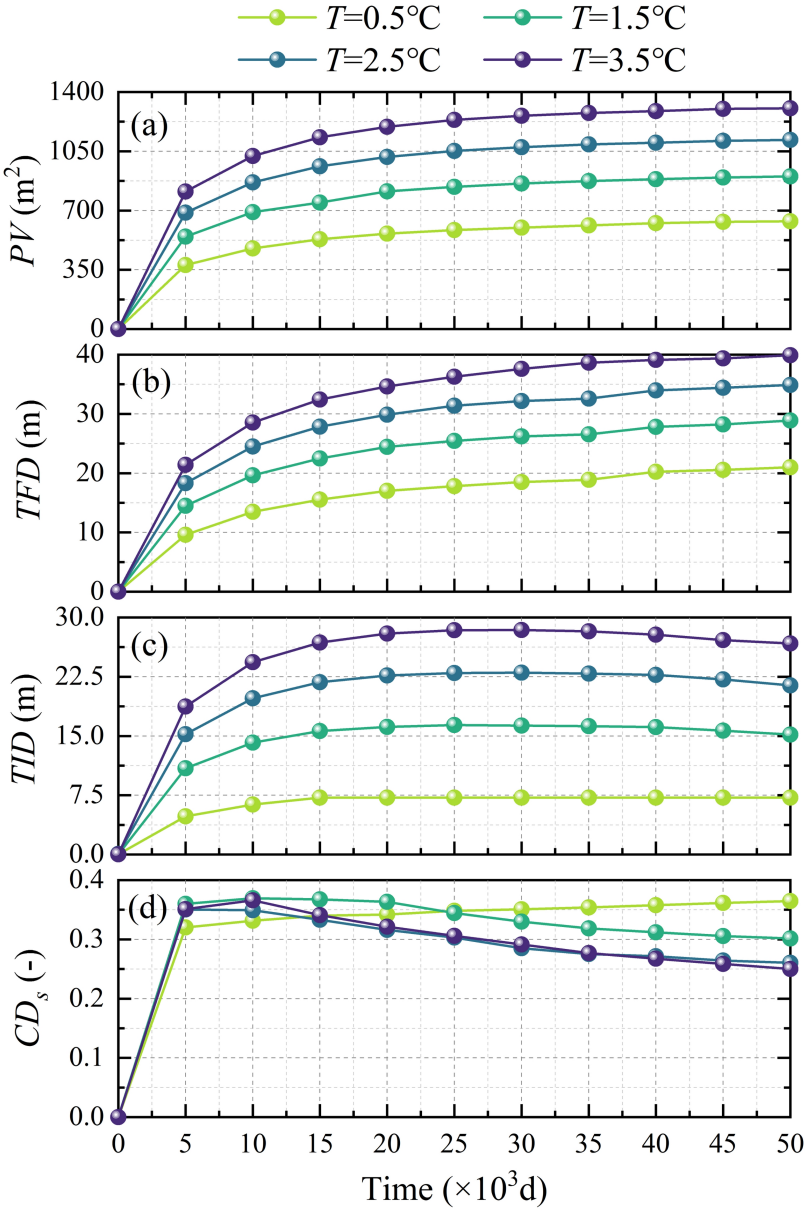


Fig. 6. Temporal variations of (a) actual permafrost thaw volume (*PV*), (b) thawing front distance (*TFD*), (c) 0 °C isotherm distance (*TID*) and (d) salt contribution degree (CD_s) under varying seawater temperatures (T_s).

https://doi.org/10.5194/egusphere-2026-5331
Preprint. Discussion started: 19 October 2026
© Author(s) 2026. CC BY 4.0 License.

3.3. Influence of aquifer hydraulic properties on thaw processes

This section examines how aquifer permeability modulates permafrost thaw driven by seawater intrusion. To illustrate the response of thaw processes to varying hydraulic properties, three representative permeability values ($k = 10^{-12}$ m^2, 10^{-11} m^2, and 10^{-10} m^2) are selected. Fig. 7 presents the coupled salinity-flow fields, water saturation, and temperature distributions under these permeabilities.

As shown in Figs. 7a$_1$, 7b$_1$, and 7c$_1$, *SWL* increases from 24.27 m to 38.10 m as k rises from 10^{-12} m^2 to 10^{-10} m^2, indicating that higher permeability promotes thaw advancement. The flow fields reveal that under the lowest permeability ($k = 10^{-12}$ m^2), only a density-driven upper (clockwise) circulation cell is present. With increasing k, a thermally-driven lower (counterclockwise) saline circulation cell emerges and expands, demonstrating that enhanced permeability improves heat-and-solute transport efficiency and shifts the dominant driving mechanism from density-driven to thermally-driven convection.

The water-saturation distributions (Figs. 7a$_2$, 7b$_2$, 7c$_2$) show that the thaw zone generally aligns with the saltwater wedge geometry. However, under the highest permeability ($k = 10^{-10}$ m^2), a wider region of incomplete thaw persists near the aquifer base. This is linked to the strengthened lower circulation cell (Fig. 7c$_1$), which diverts saline water seaward before it fully reaches the thaw front, thereby limiting local thawing. In the temperature fields (Figs. 7a$_3$, 7b$_3$, 7c$_3$), the 0 °C isotherm exhibits noticeable retreat as k increases from 10^{-12} m^2 to 10^{-10} m^2. This retreat results from the intensified lower saline circulation, which weakens inland-directed thermal convection and extends the high-temperature region toward the sea.

https://doi.org/10.5194/egusphere-2026-5331
Preprint. Discussion started: 19 October 2026
© Author(s) 2026. CC BY 4.0 License.

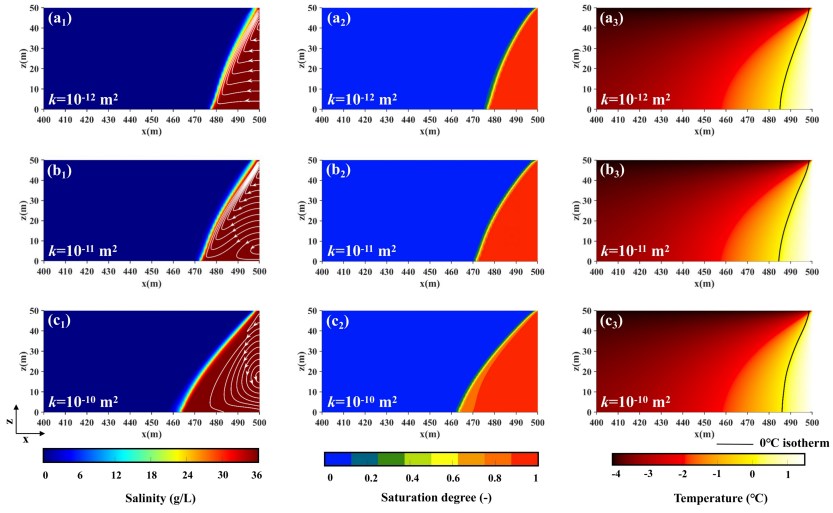


Fig. 7. Coupled flow-salinity fields, water saturation, and temperature distributions at 50,000 days under varying aquifer permeabilities (k). Panels (a_1-a_3) correspond to $k = 10^{-12}$ m^2, (b_1-b_3) to $k = 10^{-11}$ m^2, and (c_1-c_3) to $k = 10^{-10}$ m^2, showing the flow-salinity field, water saturation, and temperature field, respectively. White streamlines denote saltwater flow paths. Black lines mark the 0 °C isotherm.

The temporal evolution of key thaw metrics under varying k permeability reveals distinct dynamic responses (Fig. 8). As shown in Fig. 8a, *PV* maintains the characteristic two-stage "rapid-quasi-steady" pattern across all permeability scenarios. High k ($k = 10^{-10}$ m^2) amplifies both salinity and thermal effects, elevating the rapid-phase thawing rate to 168.8 m^2/10^3 d, but subsequently intensifies the thermally-driven lower (counterclockwise) circulation cell. This enhanced lower circulation diverts saline water seaward, reducing the stable-phase rate to 0.64 m^2/10^3 d. In contrast, low k ($k = 10^{-12}$ m^2), while reducing heat transfer efficiency, hinders the development of this lower cell, allowing more saline water to flow along the thaw front and yielding a higher stable-phase rate of 2.21 m^2/10^{3}d. *TFD* exhibits a trend consistent with *PV* (Fig. 8b). Notably, *TFD* change is

https://doi.org/10.5194/egusphere-2026-5331
Preprint. Discussion started: 19 October 2026
© Author(s) 2026. CC BY 4.0 License.

463 relatively minor for the 10^{-11} m^2 and 5×10^{-12} m^2 scenarios, indicating that despite higher heat
464 transfer efficiency in the former, the stronger constraining effect of the upper (clockwise) circulation
465 cell limits lateral thaw front advance.

466 *TID* dynamics are closely linked to the development of the lower saline circulation cell (Fig.
467 8c). Under low *k*, where no lower circulation develops within 60,000 days, *TID* shows continuous
468 inland advance without retreat. Under high *k*, *TID* first advances inland and then retreats (primarily
469 between 10,000-15,000 days), with the retreat magnitude intensifying with increasing permeability.
470 The onset time of the lower circulation (Table 2) shows a positive correlation with the timing of *TID*
471 instability. Furthermore, *TID* is smaller under high *k* due to expanded thermally-driven lower
472 circulation, which weakens inland-directed thermal convection and causes greater high-temperature
473 zone fluctuations. CD_s generally increases with *k* (Fig. 8d), approaching parity between salinity and
474 thermal effects at $k = 10^{-10}$ m^2. In low-*k* scenarios, CD_s rises continuously due to the absence of
475 lower circulation. Under high *k*, CD_s exhibits a unimodal trend, peaking at the onset of lower
476 circulation before declining—a mechanism analogous to that under elevated ocean temperatures,
477 where stronger lower circulation diverts saline water seaward, reducing its direct contribution to
478 thawing at the permafrost interface.

https://doi.org/10.5194/egusphere-2026-5331
Preprint. Discussion started: 19 October 2026
© Author(s) 2026. CC BY 4.0 License.

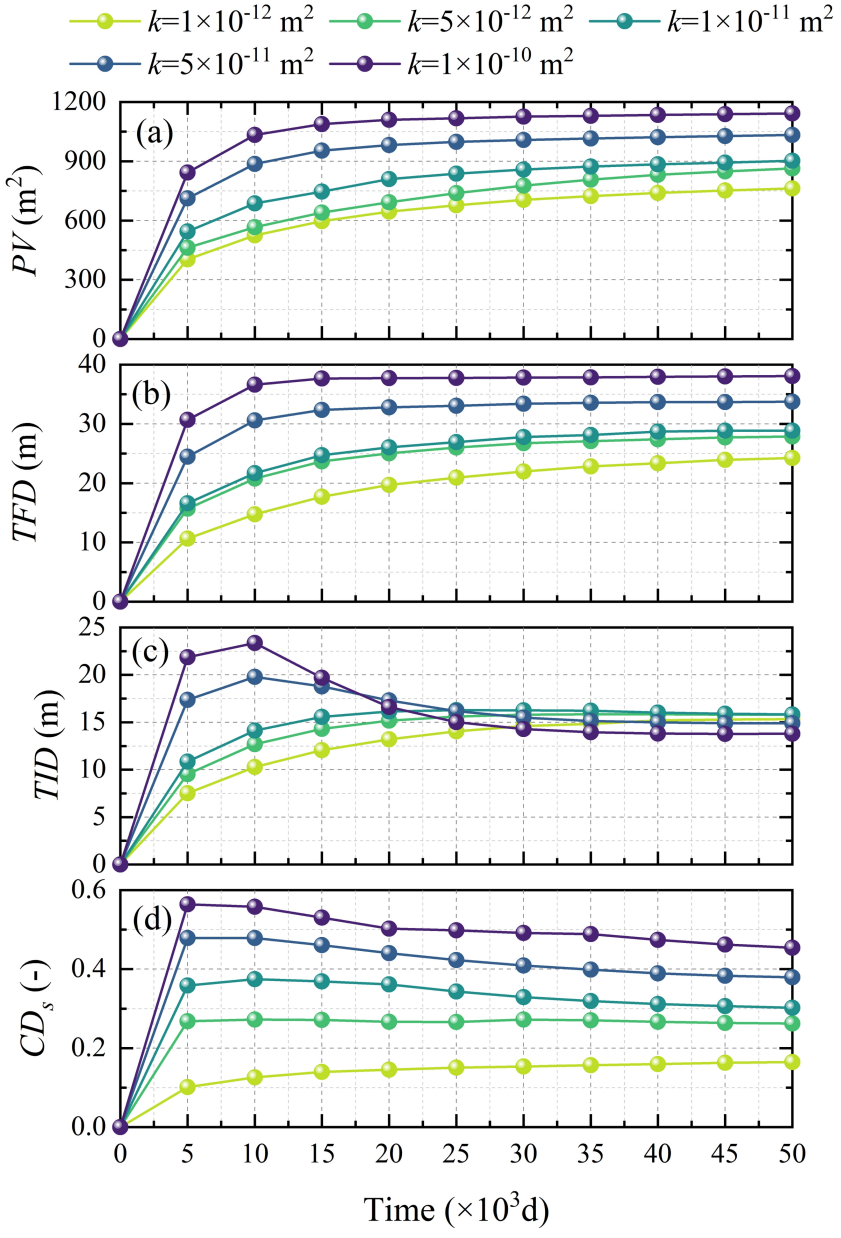


Fig. 8. Temporal variations of (a) actual permafrost thaw volume (*PV*), (b) thawing front distance (*TFD*), (c) 0 °C isotherm distance (*TID*) and (d) salt contribution degree (CD_s) under varying aquifer permeabilities (*k*).

https://doi.org/10.5194/egusphere-2026-5331
Preprint. Discussion started: 19 October 2026
© Author(s) 2026. CC BY 4.0 License.

Fig. 9 presents the coupled flow-salinity fields, water saturation, and temperature distributions at 50,000 days for porosities of n = 0.25, 0.30, 0.35, and 0.40. As shown in Figs. 9a_1-d_1, the gross morphology of the saltwater wedge exhibits limited sensitivity to porosity variations, maintaining its characteristic convex shape across all scenarios, which suggests that the primary density-driven flow pattern governing the wedge's geometry is not fundamentally reshaped by changes in pore space volume. However, a clear inverse relationship emerges for *SWL*, which increases from 27.28 m to 32.72 m as porosity decreases from n = 0.40 to n = 0.25. The water-saturation distributions (Figs. 9a_2-d_2) reveal that the spatial extent of the thaw zone remains largely unchanged with increasing porosity, indicating limited control of porosity on the phase-change field's geometry, while the position of the 0 °C isotherm in the temperature fields (Figs. 9a_3-d_3) shows minimal variation, confirming a negligible effect of porosity on the thermal field's spatial distribution under the simulated long-term conditions. These observed trends can be explained by two competing mechanisms modulated by porosity. First, lower porosity is associated with an enhanced thermally driven lower (counterclockwise) saline circulation cell—similar to the patterns observed under high permeability (Fig. 7c_1) and elevated ocean temperatures (Figs. 5c_1-d_1)—which diverts saline water seaward and weakens inland-directed thermal convection. Second, because the bulk volumetric ice content is proportional to nS_i, lower porosity reduces the volume of ice per unit bulk volume when ice saturation is comparable, thereby lowering the latent-heat demand per unit bulk volume for phase change. These two opposing effects — enhanced thermal convection versus reduced latent-heat demand—largely offset each other, resulting in limited net effects on both thaw-zone geometry and the 0 °C isotherm position (Figs. 9a_2-d_2 and 9a_3-d_3).

https://doi.org/10.5194/egusphere-2026-5331
Preprint. Discussion started: 19 October 2026
© Author(s) 2026. CC BY 4.0 License.

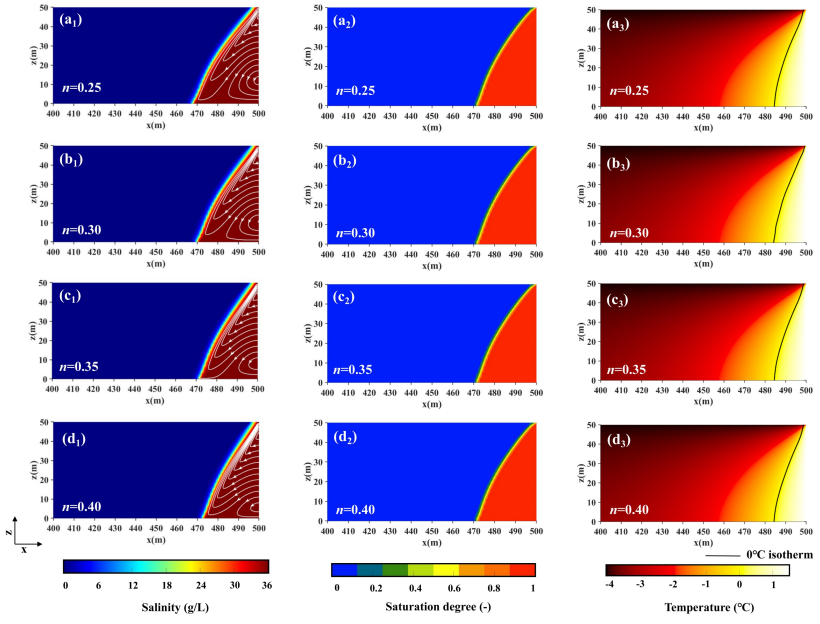


Fig. 9. Coupled flow-salinity fields, water saturation, and temperature distributions at 50,000 days under varying aquifer porosities (n). Panels (a_1-a_3) correspond to n = 0.25, (b_1-b_3) to n = 0.30, (c_1-c_3) to n = 0.35, and (d_1-d_3) to n = 0.40, showing the flow-salinity field, water saturation, and temperature field, respectively. White streamlines denote saltwater flow paths. Black lines mark the 0 °C isotherm.

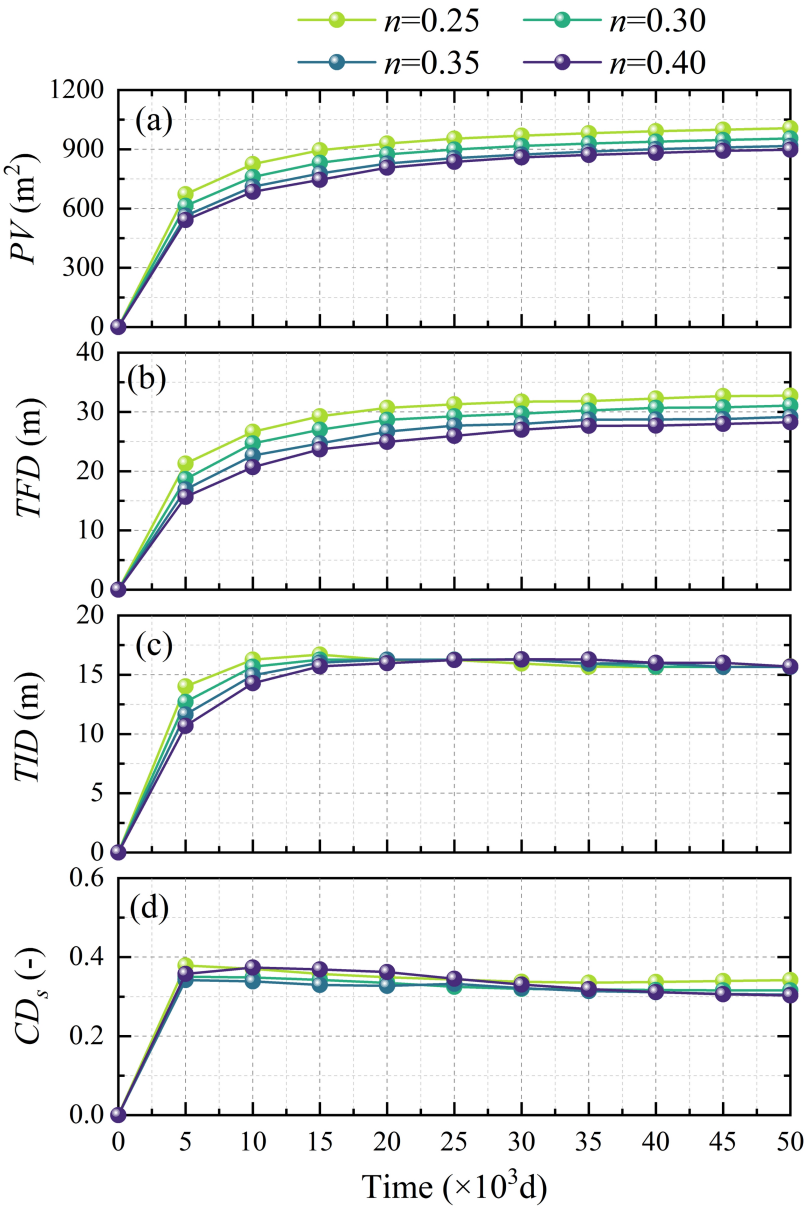
The temporal evolution of key thaw metrics under varying n reveals distinct patterns governed by competing mechanisms (Fig. 10). During the rapid thawing phase, PV thawing rate increases from 109.3 to 134.5 $m^2/10^3$ d as n decreases from 0.40 to 0.25, primarily due to reduced initial ice content and lower latent heat demand. In the stable phase, thawing rates show a non-monotonic trend (1.9, 1.74, 1.58, and 1.8 $m^2/10^3$ d for n = 0.25 to 0.40), indicating a competition between two effects: within the medium n range (n = 0.40–0.35), the inhibitory effect of the enhanced lower (counterclockwise) saline circulation cell—which diverts saline water seaward—outweighs the

https://doi.org/10.5194/egusphere-2026-5331
Preprint. Discussion started: 19 October 2026
© Author(s) 2026. CC BY 4.0 License.

promoting effect of reduced ice content; as n further decreases (n = 0.35–0.25), reduced ice content becomes dominant, leading to a renewed increase in thawing rate. *TFD* displays consistent dynamics (Fig. 10b).

TID evolution comprises rapid inland advance followed by retreat, with retreat magnitude intensifying as n decreases (Fig. 10c). This confirms that reduced n amplifies the thermal effect, strengthening the lower saline circulation cell. The variation in t_{dc} provides direct evidence: t_{dc} occurs earlier with decreasing n (21,000 d, 26,000 d, 31,000 d, and 37,000 d for n = 0.25, 0.30, 0.35, and 0.40, respectively; Table 2). This earlier development under lower n is driven by reduced ice content (lower latent heat demand) and enhanced thermal convection efficiency, accelerating the transition to the mature double-circulation system. The enhanced lower circulation weakens inland-directed thermal convection, causing pronounced seaward shift of the high-temperature region and *TID* retreat. CD_s exhibits a unimodal trend with decreasing n, first declining then rising (Fig. 10d). Initially, lower n enhances lower circulation, diverting saline water seaward and decreasing CD_s. As n further decreases, significantly reduced ice content lowers thawing enthalpy demand, increasing the relative importance of salt in depressing the freezing point and leading to a rise in CD_s.

https://doi.org/10.5194/egusphere-2026-5331
Preprint. Discussion started: 19 October 2026
© Author(s) 2026. CC BY 4.0 License.



532

533 Fig. 10. Temporal variations of (a) actual permafrost thaw volume (*PV*), (b) thawing front distance

534 (*TFD*), (c) 0 °C isotherm distance (*TID*) and (d) salt contribution degree (CD_s) under varying aquifer

535 porosities (*n*).

https://doi.org/10.5194/egusphere-2026-5331
Preprint. Discussion started: 19 October 2026
© Author(s) 2026. CC BY 4.0 License.

4. Discussion

Our results demonstrate that seawater temperature exerts a dominant control on thaw dynamics, with *PV* increasing by ~105% as Ts rises from 0.5°C to 3.5°C, and the incremental thaw rate diminishing at higher temperatures—indicating a nonlinear response. This thermal dominance is confirmed by the consistently low contribution degree of salinity ($CD_s < 0.5$) across all scenarios. These findings build upon a growing body of work on thermo-haline processes in coastal aquifers and subsea permafrost, and we clarify below what the present model adds beyond existing frameworks.

A key outcome of our model is the emergence of a double circulation cell (clockwise and counterclockwise) driven by thermal convection, which redirects saline water seaward and delays inland thaw front advance. This mechanism differs from the purely diffusive framework of Angelopoulos et al. (2019), whose field-validated heat-salt diffusion model for subsea permafrost explicitly called for the inclusion of convective transport to explain observed thaw rates. Our results answer that call: the modeled ice-bearing permafrost table depth after 1400 years of inundation (16.7 m with salt diffusion) matches their field data only when advection is included, whereas a purely diffusive scenario underpredicts thaw by ~27%. Furthermore, the double circulation we observe is not merely a consequence of double diffusion as reported by Pu et al. (2020) for non-freezing confined aquifers; in our permafrost system, the transition from single to double circulation occurs at a lower temperature contrast (~3°C) than their ~5°C threshold, because phase change reduces the effective thermal diffusivity and sharpens the density gradient. This phase-change modulation is absent in Pu et al.'s framework. Similarly, while Guimond et al. (2021, 2022) incorporated salinity-dependent freeze-thaw and solute exclusion, their simulations did not report the double circulation

https://doi.org/10.5194/egusphere-2026-5331
Preprint. Discussion started: 19 October 2026
© Author(s) 2026. CC BY 4.0 License.

cell, likely due to differences in boundary conditions or parameter ranges, and they did not isolate the relative contributions of thermal versus salinity effects—a gap our CD_s metric directly addresses. Finally, Frederick & Buffett (2015) developed a fully coupled water – heat – mass model for the Beaufort Sea shelf, but their continental-scale approach with simplified seasonal forcing could not capture the seasonal freeze-thaw cycle or double-diffusive convection resolved here. Together, these comparisons highlight that our two-dimensional, advection-coupled framework with phase change provides a mechanistic explanation for thaw patterns that previous models—whether diffusion-only (Angelopoulos et al., 2019), non-freezing (Pu et al., 2020), or shelf-scale (Frederick & Buffett, 2015)—could not fully capture.

Comparisons with recent studies on cold-region dynamics further contextualize our findings. Li et al. (2026) demonstrated that freeze-thaw in saline terrestrial soils can induce convective fingering, enhancing downward salt transport. While their focus was on seasonal freeze-thaw in unsaturated zones, the role of gravitational instabilities parallels our observation of double circulation cells. However, in our coastal system, ocean warming provides a persistent thermal forcing that overwhelms salinity effects over time ($CD_s < 0.5$), whereas Li et al. (2026) emphasized salt-driven convection in the absence of sustained thermal gradients. Yu et al. (2026) showed that frozen ground in coastal aquifers confines flow paths and accelerates terrestrial groundwater discharge, but their steady-state analysis omitted phase-change dynamics. Our model explicitly couples thaw-induced changes in relative permeability and the resulting changes in effective hydraulic conductivity with evolving flow patterns, suggesting that the dual circulation cell generates a flow confinement effect similar to that observed by Yu et al. (2026), but is driven primarily by thermal convection rather than by reduced permeability in frozen ground alone. This

https://doi.org/10.5194/egusphere-2026-5331
Preprint. Discussion started: 19 October 2026
© Author(s) 2026. CC BY 4.0 License.

distinction is critical for predicting thaw rates under transient warming scenarios.

Quantification of CD_s and t_{dc} provides practical metrics for assessing infrastructure vulnerability and carbon mobilization in Arctic aquifers. However, our model assumes homogeneous aquifer properties and a closed inland hydraulic boundary; future work should incorporate heterogeneity, seasonal variability, and erosion processes. Nonetheless, by bridging the diffusion-based approach of Angelopoulos et al. (2019) and the non-freezing double-diffusion theory of Pu et al. (2020), our study offers a unified framework for predicting multi-physical interactions in coastal permafrost under climate change.

5. Conclusions

This numerical study elucidates the complex thermo-hydro-saline coupling processes governing coastal permafrost thaw driven by seawater intrusion. The key findings and their implications are summarized as follows:

(1) Seawater temperature (T_s) is the primary driver of thaw acceleration. Warmer ocean water intensifies thermal convection and solute transport, leading to a nonlinear increase in permafrost thaw volume —approximately 105% growth as T_s rises from 0.5°C to 3.5°C. The earlier onset of a thermally-driven, counterclockwise saline circulation cell under higher T_s (t_{dc} decreasing from 55,000 to 25,000 days) fundamentally reshapes long-term flow and heat transfer, establishing ocean warming as a critical amplifier of coastal permafrost degradation.

(2) The evolution from single to double saline circulation governs the thermal-solute coupling. The system transitions from an initial density-driven, clockwise cell to a mature double-circulation pattern. This transition, quantified by the salt contribution degree ($CD_s < 0.5$), reveals that thermal forcing dominates thaw, while salinity primarily modulates early-phase thawing by depressing the

https://doi.org/10.5194/egusphere-2026-5331
Preprint. Discussion started: 19 October 2026
© Author(s) 2026. CC BY 4.0 License.

freezing point. The later-stage counterclockwise cell diverts saline water seaward, attenuating inland-directed thermal convection and causing retreat of the 0°C isotherm, a key feedback mechanism not captured in prior models.

(3) Aquifer hydraulic properties strongly modulate thaw sensitivity and patterns. Higher permeability accelerates thaw by enhancing heat and solute transport but also promotes the earlier development of the counterclockwise circulation, which can limit further inland advance. Lower porosity reduces latent heat demand, increasing initial thaw rates, but its net effect is balanced by enhanced thermal convection.

These findings demonstrate that coastal permafrost vulnerability is highly sensitive to projected ocean warming and subsurface properties. The quantified relationships among ocean temperature, aquifer parameters, and thaw metrics provide a scientific basis for improving forecasts of carbon mobilization from thawing permafrost and for assessing geotechnical risks to Arctic coastal infrastructure. Future work should incorporate more complex boundary conditions, such as tidal fluctuations, seasonal variability, and heterogeneous aquifer structures, to refine predictions under realistic environmental scenarios.

Acknowledgements

This work was supported by the National Natural Science Foundation of China (No. 42422207) and Taishan Scholars Program of Shandong Province (No. tsqn202408078).

Author contributions

TYZ: Conceptualization, Methodology, Software, Resources, Writing-Original Draft, Writing-Review and Editing, Funding acquisition, Supervision.

https://doi.org/10.5194/egusphere-2026-5331
Preprint. Discussion started: 19 October 2026
© Author(s) 2026. CC BY 4.0 License.

623 YCL: Investigation, Software, Writing-Review and Editing, Visualization, Data Curation.

624 SBG: Methodology, Formal Analysis, Investigation, Visualization, Writing-Review and Editing.

625 XLZ: Investigation, Visualization, Writing-Review and Editing.

626 RH: Formal Analysis, Investigation, Writing-Review and Editing.

627 JL: Conceptualization, Methodology, Writing-Review and Editing, Supervision.

628 **Competing interests**

629 Some authors are members of the editorial board of *Hydrology and Earth System Sciences*.

630 ## Code and data availability

631 The data can be found: https://doi.org/10.5281/zenodo.22242291.

https://doi.org/10.5194/egusphere-2026-5331
Preprint. Discussion started: 19 October 2026
© Author(s) 2026. CC BY 4.0 License.

References

Angelopoulos, M., Westermann, S., Overduin, P., Faguet, A., Olenchenko, V., Grosse, G., & Grigoriev, M. N. (2019). Heat and salt flow in subsea permafrost modeled with CryoGRID2. Journal of Geophysical Research: Earth Surface, 124(4), 920-937. https://doi.org/10.1029/2018JF004823

Bense, V. F., Ferguson, G., & Kooi, H. (2009). Evolution of shallow groundwater flow systems in areas of degrading permafrost. Geophysical Research Letters, 36(22). https://doi.org/10.1029/2009GL039225

Bense, V. F., Kooi, H., Ferguson, G., & Read, T. (2012). Permafrost degradation as a control on hydrogeological regime shifts in a warming climate. Journal of Geophysical Research: Earth Surface, 117(F3). https://doi.org/10.1029/2011JF002143

Demir, C., McClelland, J. W., Bristol, E., Charette, M. A., & Cardenas, M. B. (2024). Coastal supra-permafrost aquifers of the Arctic and their significant groundwater, carbon, and nitrogen fluxes. Geophysical Research Letters, 51(22), e2024GL109142. https://doi.org/10.1029/2024GL109142

Devoie, É., Connon, R. F., Beddoe, R., Goordial, J., Quinton, W. L., & Craig, J. R. (2024). Disconnected active layers and unfrozen permafrost: A discussion of permafrost-related terms and definitions. Science of the Total Environment, 912, 169017. https://doi.org/10.1016/j.scitotenv.2023.169017

England, M. R., Eisenman, I., Lutsko, N. J., & Wagner, T. J. (2021). The recent emergence of Arctic amplification. Geophysical Research Letters, 48(15), e2021GL094086. https://doi.org/10.1029/2021GL094086

https://doi.org/10.5194/egusphere-2026-5331
Preprint. Discussion started: 19 October 2026
© Author(s) 2026. CC BY 4.0 License.

654 Frampton, A., & Destouni, G. (2015). Impact of degrading permafrost on subsurface solute transport
655 pathways and travel times. Water Resources Research, 51(9), 7680-7701.
656 https://doi.org/10.1002/2014WR016689
657 Frederick, J. M., & Buffett, B. A. (2015). Effects of submarine groundwater discharge on the present
658 - day extent of relict submarine permafrost and gas hydrate stability on the Beaufort Sea
659 continental shelf. Journal of Geophysical Research: Earth Surface, 120(3), 417-432.
660 https://doi.org/10.1002/2014JF003349
661 Gao, S., Zheng, T., Zheng, X., & Luo, J. (2025). Impact of river-groundwater interactions on residual
662 saltwater pollution in estuarine groundwater reservoirs. Water Research, 279, 123474.
663 https://doi.org/10.1016/j.watres.2025.123474
664 Guimond, J. A., Mohammed, A. A., Walvoord, M. A., Bense, V. F., & Kurylyk, B. L. (2021).
665 Saltwater intrusion intensifies coastal permafrost thaw. Geophysical Research Letters, 48(19),
666 e2021GL094776. https://doi.org/10.1029/2021GL094776
667 Guimond, J. A., Mohammed, A. A., Walvoord, M. A., Bense, V. F., & Kurylyk, B. L. (2022). Sea-
668 level rise and warming mediate coastal groundwater discharge in the Arctic. Environmental
669 Research Letters, 17(4), 045027. https://doi.org/10.1088/1748-9326/ac6085
670 Harrison, W. D., & Osterkamp, T. E. (1978). Heat and mass transport processes in subsea permafrost
671 1. An analysis of molecular diffusion and its consequences. Journal of Geophysical Research:
672 Oceans, 83(C9), 4707-4712. https://doi.org/10.1029/JC083iC09p04707
673 Hjort, J., Streletskiy, D., Doré, G., Wu, Q., Bjella, K., & Luoto, M. (2022). Impacts of permafrost
674 degradation on infrastructure. Nature Reviews Earth & Environment, 3(1), 24-38.
675 https://doi.org/10.1038/s43017-021-00247-8

https://doi.org/10.5194/egusphere-2026-5331
Preprint. Discussion started: 19 October 2026
© Author(s) 2026. CC BY 4.0 License.

Johnson, G. C., & Lyman, J. M. (2020). Warming trends increasingly dominate global ocean. Nature Climate Change, 10(8), 757-761. https://doi.org/10.1038/s41558-020-0822-0

Jones, M. C., Grosse, G., Treat, C., Turetsky, M., Anthony, K. W., & Brosius, L. (2023). Past permafrost dynamics can inform future permafrost carbon-climate feedbacks. Communications Earth & Environment, 4(1), 272. https://doi.org/10.1038/s43247-023-00886-3

Kasprzak, M., Strzelecki, M. C., Traczyk, A., Kondracka, M., Lim, M., & Migała, K. (2017). On the potential for a bottom active layer below coastal permafrost: The impact of seawater on permafrost degradation imaged by electrical resistivity tomography (Hornsund, SW Spitsbergen). Geomorphology, 293, 347-359. https://doi.org/10.1016/j.geomorph.2016.06.013

Kuan, W. K., Xin, P., Jin, G., Robinson, C. E., Gibbes, B., & Li, L. (2019). Combined effect of tides and varying inland groundwater input on flow and salinity distribution in unconfined coastal aquifers. Water Resources Research, 55(11), 8864-8880. https://doi.org/10.1029/2018WR024492

Lamontagne-Hallé, P., McKenzie, J. M., Kurylyk, B. L., Molson, J., & Lyon, L. N. (2020). Guidelines for cold-regions groundwater numerical modeling. Wiley Interdisciplinary Reviews: Water, 7(6), e1467. https://doi.org/10.1002/wat2.1467

Larsen, J. N., Schweitzer, P., Abass, K., Doloisio, N., Gartler, S., Ingeman-Nielsen, T., Ingimundarson, J., Jungsberg, L., Meyer, A., Rautio, A., Scheer, J., Timlin, U., Vanderlinden, J., & Vullierme, M. (2021). Thawing permafrost in Arctic coastal communities: a framework for studying risks from climate change. Sustainability, 13(5), 2651. https://doi.org/10.3390/su13052651

https://doi.org/10.5194/egusphere-2026-5331
Preprint. Discussion started: 19 October 2026
© Author(s) 2026. CC BY 4.0 License.

Li, Y., Wu, J., Tian, H., Yu, X., & Xin, P. (2026). Freeze-thaw processes induce convective fingering in saline soils. Geophysical Research Letters, 53(1), e2025GL119845. https://doi.org/10.1029/2025GL119845

Lindsey, R., & Dahlman, L. (2020). Climate change: Global temperature. Climate. gov, 16, 1-5.

Lu, C., Xin, P., Kong, J., Li, L., & Luo, J. (2016). Analytical solutions of seawater intrusion in sloping confined and unconfined coastal aquifers. Water Resources Research, 52(9), 6989-7004. https://doi.org/10.1002/2016WR019101

McKenzie, J. M., Voss, C. I., & Siegel, D. I. (2007). Groundwater flow with energy transport and water–ice phase change: Numerical simulations, benchmarks, and application to freezing in peat bogs. Advances in water resources, 30(4), 966-983. https://doi.org/10.1016/j.advwatres.2006.08.008

Mohammed, A. A., Bense, V. F., Kurylyk, B. L., Jamieson, R. C., Johnston, L. H., & Jackson, A. J. (2021). Modeling reactive solute transport in permafrost-affected groundwater systems. Water Resources Research, 57(7), e2020WR028771. https://doi.org/10.1029/2020WR028771

Nguyen, T. T., Yu, X., Pu, L., Xin, P., Zhang, C., Barry, D. A., & Li, L. (2020). Effects of temperature on tidally influenced coastal unconfined aquifers. Water Resources Research, 56(4), e2019WR026660. https://doi.org/10.1029/2019WR026660

Pachauri, R. K., & Reisinger, A. (2007). IPCC fourth assessment report. IPCC, Geneva, 2007(673), 044023.

Pu, L., Xin, P., Nguyen, T. T., Yu, X., Li, L., & Barry, D. A. (2020). Thermal effects on flow and salinity distributions in coastal confined aquifers. Water Resources Research, 56(10), e2020WR027582. https://doi.org/10.1029/2020WR027582

https://doi.org/10.5194/egusphere-2026-5331
Preprint. Discussion started: 19 October 2026
© Author(s) 2026. CC BY 4.0 License.



720 Robinson, C., Li, L., & Barry, D. A. (2007). Effect of tidal forcing on a subterranean estuary.
721 Advances in Water Resources, 30(4), 851-865.
722 https://doi.org/10.1016/j.advwatres.2006.07.006
723 Steinert, N. J., Debolskiy, M. V., Burke, E. J., García-Pereira, F., & Lee, H. (2023). Evaluating
724 permafrost definitions for global permafrost area estimates in CMIP6 climate models.
725 Environmental Research Letters, 19(1), 014033. https://doi.org/10.1088/1748-9326/ad10d7
726 Walvoord, M. A., & Kurylyk, B. L. (2016). Hydrologic impacts of thawing permafrost—A review.
727 Vadose Zone Journal, 15(6), vzj2016-01. https://doi.org/10.2136/vzj2016.01.0010
728 Watanabe, K., & Osada, Y. (2016). Comparison of hydraulic conductivity in frozen saturated and
729 unfrozen unsaturated soils. Vadose Zone Journal, 15(5), vzj2015-11.
730 https://doi.org/10.2136/vzj2015.11.0154
731 Werner, A. D., Bakker, M., Post, V. E., Vandenbohede, A., Lu, C., Ataie-Ashtiani, B., Simmons, C.,
732 & Barry, D. A. (2013). Seawater intrusion processes, investigation and management: Recent
733 advances and future challenges. Advances in Water Resources, 51, 3-26.
734 https://doi.org/10.1016/j.advwatres.2012.03.004
735 Xu, L., Ma, M. Y., Lan, T. G., Wang, Y. X., & Lu, S. F. (2024). Exploring soil water retention
736 hysteresis in the entire suction range and microstructure evolution of loess: The influence of
737 sediment depths. Engineering Geology, 328, 107373.
738 https://doi.org/10.1016/j.enggeo.2023.107373
739 Yu, X., Li, Y., Pu, L., Wu, J., & Xin, P. (2026). Frozen ground induces seawater retreat in coastal
740 unconfined aquifers. Geophysical Research Letters, 53, e2025GL117947.
741 https://doi.org/10.1029/2025GL117947

https://doi.org/10.5194/egusphere-2026-5331
Preprint. Discussion started: 19 October 2026
© Author(s) 2026. CC BY 4.0 License.



742 Zhou, W., Leung, L. R., Xie, S. P., & Lu, J. (2024). An analytic theory for the degree of Arctic
743 Amplification. Nature Communications, 15(1), 5060. https://doi.org/10.1038/s41467-024-
744 48469-w